International Journal of Heat and Mass Transfer 115 (2017) 513–522

Contents lists available at ScienceDirect

International Journal of Heat and Mass Transfer

journal homepage: www.elsevier.com/locate/ijhmt

Carbon fiber composites with 2D microvascular networks for battery cooling

Stephen J. Pety [a,d], Marcus Hwai Yik Tan [b,d], Ahmad R. Najafi [b,d], Philip R. Barnett [c,d], Philippe H. Geubelle [c,d], Scott R. White [c,d,*]

[a] Department of Materials Science and Engineering, University of Illinois at Urbana-Champaign, 1304 W Green St., Urbana, IL 61801, USA
[b] Department of Mechanical Science and Engineering, University of Illinois at Urbana-Champaign, 1206 W Green St., Urbana, IL 61801, USA
[c] Department of Aerospace Engineering, University of Illinois at Urbana-Champaign, 104 S. Wright St., Urbana, IL 61801, USA
[d] Beckman Institute for Advanced Science and Technology, University of Illinois at Urbana-Champaign, 405 N Mathews Av., Urbana, IL 61801, USA

ARTICLE INFO

Article history:
Received 16 March 2017
Received in revised form 30 June 2017
Accepted 10 July 2017

Keywords:
Battery cooling
Microvascular composites
Carbon fiber
Computational fluid dynamics
Thermal imaging
Multifunctional materials

ABSTRACT

Electric vehicle (EV) batteries require both thermal regulation and crash protection. A novel battery packaging scheme is presented that uses microvascular composite panels with 2D channel networks to accomplish both objectives. Microvascular carbon fiber/epoxy composite panels are fabricated by vacuum assisted resin transfer molding, with the channel network formed by post-cure vaporization of an embedded polylactide channel template. Panel cooling performance is evaluated for parallel, bifurcating, serpentine, and spiral channel designs at different coolant flow rates and channel diameter. The spiral design provides the best thermal performance, but requires high pumping pressure (>100 kPa) at the flow rates needed for adequate cooling (>30 mL min^{-1}). The bifurcating design and a network obtained by computational optimization offer much lower pressure with slightly reduced thermal performance. Channel diameter has negligible effect on cooling performance, but strongly affects pumping pressure. Computational fluid dynamics (CFD) simulations are also performed and correlate well with the experimental data. Simulations confirm that microvascular composite panels can cool typical battery cells generating 500 W m^{-2} heat flux below the target temperature of 40 °C.

1. Introduction

A major challenge in the design of electric vehicles (EVs) is how to properly package the batteries. Plug-in EVs typically require active battery cooling, since most use lithium-ion batteries which release considerable heat during operation [1,2]. Without cooling, battery lifetime is drastically reduced due to harmful side reactions at temperatures above ca. 40 °C [3,4]. Cooling is also needed to prevent thermal runaway when a cell is suddenly damaged or short circuited [5]. Several battery cooling strategies have been developed for EVs such as cooling with liquid flow [6,7], air flow [8,9], heat pipes [10] and phase change materials [11], with liquid and air flow the most commercially successful.

Battery packaging must also provide structural protection for battery cells in the event of a crash. This requirement has led to complex packaging schemes such as that used in the Chevy Volt; liquid coolant is pumped through aluminum cooling panels with outer layers of fiberglass and steel that provide structural protection [6,7]. Despite these protection schemes, several EV battery packs have caught fire after crashes due to damaged batteries and cooling systems [12,13]. There remains a critical need for a packaging scheme that can provide simultaneous structural protection and active cooling while still maintaining light weight.

Here we propose a novel packaging scheme using microvascular carbon fiber composites where both structural protection and active cooling are accomplished in a single, lightweight material. In this scheme, battery cells are embedded within composite panels through which coolant can flow for thermal management (Fig. 1a). Batteries can be stacked in a central pack, with additional composite reinforcement encompassing the pack exterior as needed (Fig. 1b). Alternatively, batteries can be integrated within structural carbon fiber body panels throughout the vehicle. Either scheme provides systems-level savings of volume and weight [14,15] and superior crash protection at low weight [16].

Several strategies exist to manufacture microvascular fiber-reinforced composites, including the use of hollow glass fibers

* Corresponding author at: Department of Aerospace Engineering, University of Illinois at Urbana-Champaign, 104 S. Wright St., Urbana, IL 61801, USA.

E-mail addresses: pety1@illinois.edu (S.J. Pety), htan8@illinois.edu (M.H.Y. Tan), arnajafi@illinois.edu (A.R. Najafi), pbarnet3@tennessee.edu (P.R. Barnett), geubelle@illinois.edu (P.H. Geubelle), swhite@illinois.edu (S.R. White).

http://dx.doi.org/10.1016/j.ijheatmasstransfer.2017.07.047
0017-9310/

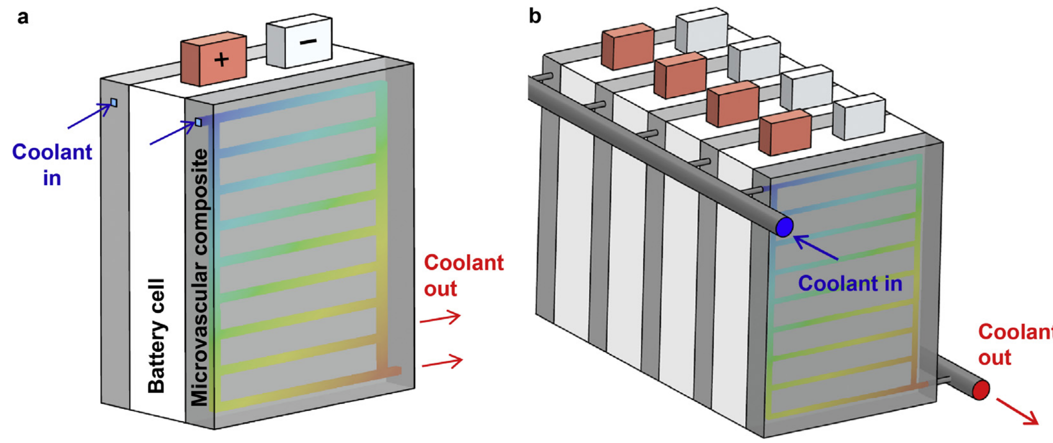

Fig. 1. Schematic of battery packaging using microvascular composite panels with 2D channel networks. (a) Battery cell is sandwiched between microvascular composite panels through which liquid coolant is pumped. (b) Multiple battery cells are assembled into a battery pack with an integrated coolant distribution manifold.

[17,18], extraction of steel wires [19,20], melting of embedded solder [21,22], and the vaporization of sacrificial components (VaSC) [23–29]. In the VaSC technique, catalyst-treated polylactide (PLA) is incorporated into a composite layup and vaporized after cure. VaSC is particularly attractive since it is scalable and can form channel networks with a variety of complex, interconnected architectures. Vascular networks enable efficient thermal management of composites [27–33] as well as other functionalities such as self-healing [24,34] and damage sensing [35].

While microchannels enable composites with multifunctionality, their incorporation can potentially reduce composite mechanical properties. As reviewed by Saeed et al. [36], many studies have characterized how microchannels affect properties such as tensile/compressive strength and stiffness [26,37–39], mode 1 and mode 2 fracture toughness [21], low-velocity impact response [40], and interlaminar shear strength [41]. Mechanical properties are typically preserved when channel volume fraction is low (<2%) and when channels do not disrupt the architecture or continuity of load-bearing plies. Pety and coworkers [42] also recently confirmed that up to 4 vol% of microchannels can be incorporated into composite panels without decreasing their crashworthiness. Crush tests on microvascular panels revealed no loss in specific energy absorbed (SEA) for channels both aligned and misaligned with the loading direction.

Microvascular composite panels for battery cooling were first studied by Pety et al. [42]. Experiments were conducted on panels with straight, isolated microchannels while the panels were subject to a heat flux representative of an EV battery. Both experimental results and computational fluid dynamics (CFD) simulations confirm that microvascular carbon/epoxy composite panels can adequately cool batteries in an EV pack above a minimum channel density and flow rate.

While all prior studies are limited to arrays of straight channels, here we implement recent advances in the VaSC processing technique [25] to create composites with 2D interconnected and branched microchannel networks for battery cooling. Two-dimensional vascular networks can be designed for spatially varying thermal fields and localized hot spots, while network branching offers the benefit of redundancy to circumvent channel blockages.

Few studies have compared different channel network designs for battery cooling [43,44]. More insight can be gained from related work on fuel cell cooling [45–48]. Studies have been performed on single-channel designs (e.g. serpentine and spiral networks) and on branched designs (e.g. parallel, bifurcating, etc.). Single-channel designs typically give better thermal performance than branched designs at the expense of higher pumping power (and pressure) [45,46]. Spiral networks, in particular, tend to give very uniform temperature fields [47]. For branched designs, bifurcating networks typically outperform parallel networks due to better flow distribution [48].

In this study, cooling performance was compared for carbon fiber panels with parallel, bifurcating, serpentine, and spiral channel networks. The total channel volume fraction was limited to <1.6% in order to preserve mechanical properties of the composite. Cooling experiments with an IR camera and CFD simulations using ANSYS Fluent were used to compare different designs. The effect of channel size was studied for the bifurcating network, and the parallel design was improved using a gradient-based computational optimization technique [49]. Finally, simulations were performed that are representative of typical operating conditions for an EV battery pack.

2. Methods

2.1. Fabrication and testing of microvascular composite panels

2.1.1. Fabrication of sacrificial PLA networks

PLA polymer blended with 3 wt% of tin(II) oxalate catalyst (CU Aerospace) was pressed into sheets using a hot press (Tetrahedron model MP-13). Press conditions were 160 °C and 960 kPa for 10 min, with sheet thickness controlled by aluminum shims. Average sheet thickness was 840 μm with a standard deviation of 40 μm, based on 32 measurements across 4 networks.

Sheets were cut into 2D network templates (Fig. 2a) using a 90 W CO_2 laser cutter (Full Spectrum Laser, Pro Series, 48″ × 36″). Network templates were designed in SolidWorks 2014 and the laser cutter was controlled using RetinaEngrave (2011) software. Three passes of the cutter were performed (at 100% speed, 4% power) to provide a complete cut with minimal edge charring. The average network width was 1020 μm with a standard deviation of 80 μm, based on 90 measurements across 4 networks. After a network template was cut from a sheet, the scrap material was recycled for reuse.

Four network designs were created (Fig. 3) which are denoted as the parallel, bifurcating, serpentine, and spiral designs. These networks provide channel volume fractions of 1.3–1.5% and channel lengths up to 1.6 m for the bifurcating design. To study the effect of channel size, one bifurcating network was also created at a reduced channel size of 570 ± 70 μm wide and 500 ± 10 μm thick. This network yields a channel volume fraction of 0.5%.

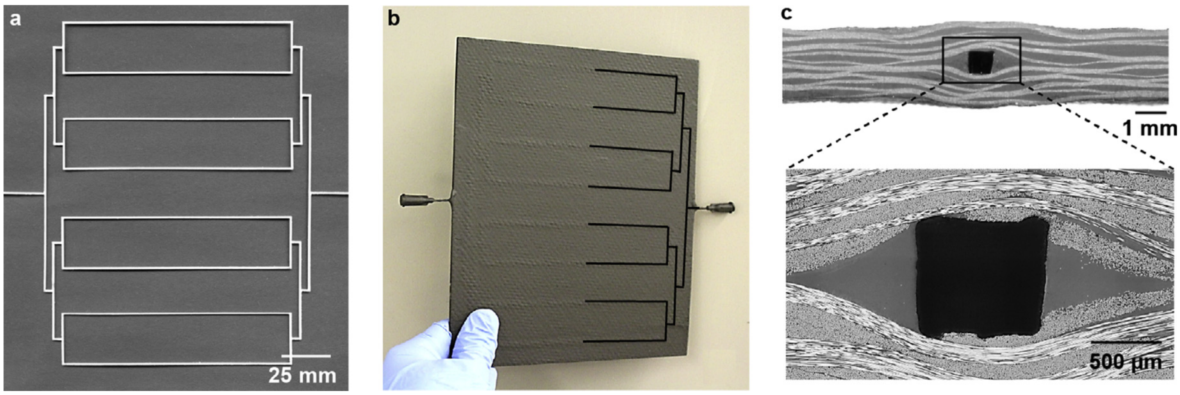

Fig. 2. Carbon fiber/epoxy composite panels with 2D channel networks. (a) Laser-cut PLA network with the bifurcating channel design. The network is 840 µm thick and strips are 1020 µm wide. (b) Composite panel with bifurcating channel network after curing and VaSC treatment. The right half of the embedded network is outlined in black for visualization. (c) Cross-sectional micrograph of a 1020 µm × 840 µm rectangular channel embedded in a carbon/epoxy composite.

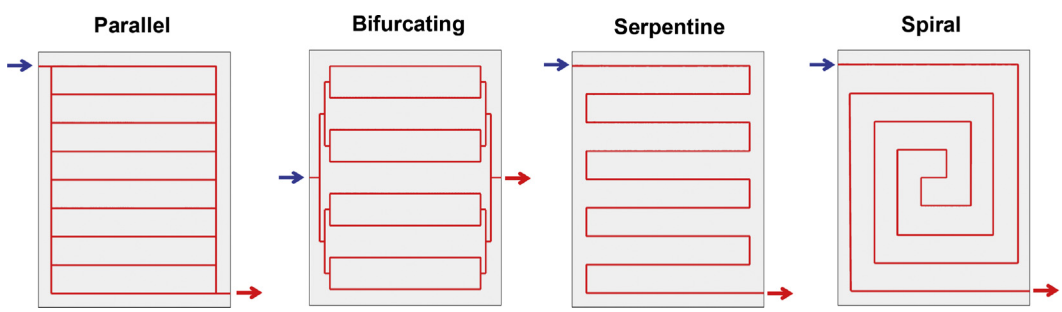

Fig. 3. Four main network designs used for cooling studies, with inlets denoted in blue (→) and outlets in red (→).

2.1.2. Fabrication of microvascular composite panels

Microvascular carbon/epoxy composite panels were prepared using vacuum-assisted resin transfer molding (VARTM). Twelve layers of 2 × 2 twill weave of Toray T300 3 K carbon fiber (205 g m^{-2}, Rock West Composites) were stacked in a double vacuum bag layup, with the PLA network template placed between the 6th and 7th layer (Fig. S1). Epoxy resin consisting 100:35 Araldite LY 8605 epoxide to Aradur 8605 curing agent (Huntsman Advanced Materials) was mixed by hand, degassed for at least 3 h at room temperature, and pulled through the layup using a vacuum pump at ~ 40 torr. Resin was cured at room temperature for 24 h and then 121 °C for 2 h followed by either 155 °C or 177 °C for 3 h. The heating rate was 2 °C min^{-1} and the cooling rate to ambient was 1 °C min^{-1}. The final cure temperature was reduced to 155 °C after it was observed that the PLA template was prematurely vaporizing during the 177 °C step. The final degree of cure was unaffected by this change in the cure cycle.

Average panel thickness was 2.96 ± 0.23 mm which corresponds to a fiber volume fraction of 45.4 ± 3.3% based on ASTM D3171 (Test Method II). After cure, composite panels were cut to size with a diamond saw (MK TX3) and subject to VaSC at 200 °C and vacuum (ca. 1 torr) for 24 h to vaporize the PLA. This process yields channel networks that are the inverse replica of the PLA network template (Fig. 2b). The microchannels have a rectangular cross-section with slightly rounded corners, as shown in cross-sections for a 1020 µm × 840 µm channel in Fig. 2c and for a 570 µm × 500 µm channel in Fig. S2.

2.1.3. Thermal testing of composites

Holes 1.03 mm in diameter were drilled 3 mm deep into the inlet and outlet of each channel to allow for 19 gauge needle fittings to be inserted. Needle fittings were secured with a two-part epoxy (JB Weld). One surface of the panel was painted with a matte black paint (Krylon) for thermal imaging. The composite specimen was then placed in the experimental setup shown in Fig. 4a and coupled to a polyimide flexible heater (Omega, part # KH-608/2) using thermal grease (Omega, part # Omegatherm 201). The heat flux generated by the heater was controlled by adjusting voltage with a Variac variable transformer (Staco Energy Products Co., Type L1010) while monitoring the voltage with a multimeter (Fluke Inc., Model 179). Voltage values were correlated to heat flux values using the equation $q'' = V^2/RA$ where q'' is areal heat flux, V is voltage, R is the resistance of the heater (105 Ω), and A is the exposed surface area of the panel (0.03 m^2). The sides of the specimen were insulated with strips of fiberglass insulation and the top was exposed for IR imaging.

The coolant, 50:50 water:ethylene glycol (Macron Chemicals), was stored in a circulator (Julabo, Model F32-HP) at 21 °C and pumped through the composite with a peristaltic pump (Cole-Parmer Masterflex, Model EW-07551099). Thermocouple probes (Omega part # TMQSS-020U-36, ±0.5 °C) were inserted into the tubing before the inlet and after the outlet to measure coolant temperature. Thermocouple readings were processed with four-port thermocouple readers (Phidgets Inc., model #1048_0) and LabVIEW 2013. Surface temperature measurements of the panel were taken with an infrared (IR) camera (FLIR, Model SC620) with an absolute temperature accuracy of ±2 °C.

Wet/wet gage pressure transducers (Omega, part # Px26) were used to measure pressure drop through the networks. Transducers with ranges of 0–35, 0–103, and 0–207 kPa were used with accuracies of 1% full scale for each. Pressure values were recorded using a DAQ board (National Instruments, NI USB-6251) and LabVIEW. To account for the pressure drop through the needle fittings, calibration tests were performed in which coolant was pumped

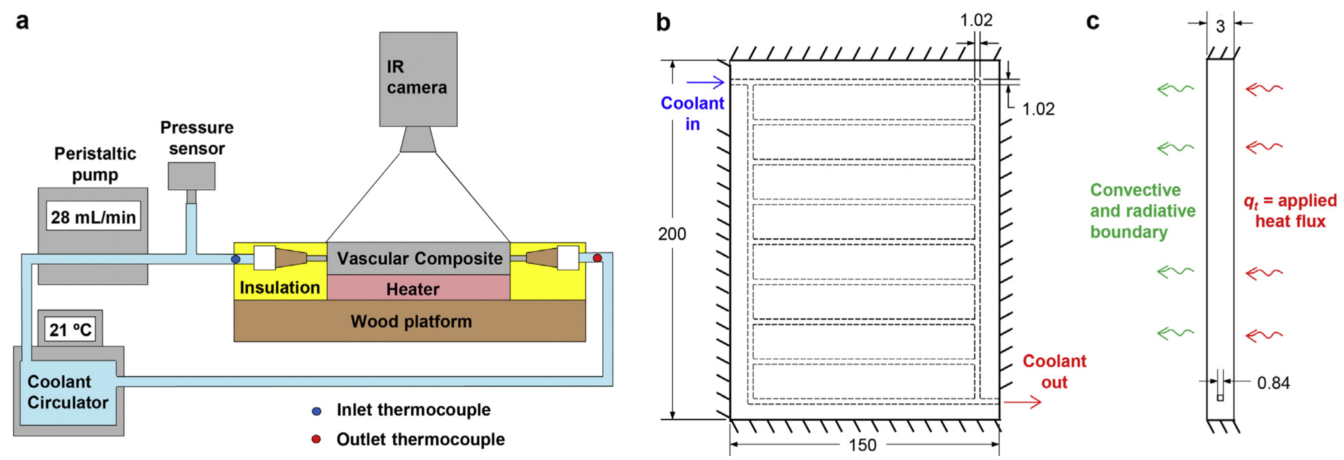

Fig. 4. Schematics of cooling experiments and simulations. (a) Experimental setup where panel surface temperature is recorded with an IR camera, coolant inlet and outlet temperature are measured with thermocouples embedded in tubing lines, and coolant pressure drop is measured with a pressure sensor. (b and c) Top and side view of simulation model (dimensions in mm). The microvascular composite panel is heated from below while coolant circulates through the channel network at a set inlet temperature and flow rate. The in-plane boundaries are thermally insulated.

through two fused needle fittings. Final pressure values for a cooling test were found by taking the raw pressure and subtracting the pressure required to pump coolant through the fittings (see Fig. S3 for the pressure adjustment vs. flow rate).

Panel surface temperature, average coolant temperature rise ΔT_c, and coolant pumping pressure at steady-state were measured during experiments. The cooling efficiency (η) of the panel was then calculated as the ratio of the heat flux absorbed by the channels (q_c) to the total heat flux applied (q_t),

$$\eta = \frac{q_c}{q_t} = \frac{\dot{m} c_p \Delta T_c}{q_t} \tag{1}$$

where $\dot{m}$ is coolant flow rate and c_p is the specific heat of the coolant.

2.2. CFD simulations in ANSYS fluent

2.2.1. Simulation setup and boundary conditions

The commercial computational fluid dynamics (CFD) package ANSYS Fluent v15.0 was used to simulate the cooling performance of microvascular panels. Panel dimensions and boundary conditions imposed are specified in Fig. 4b and c. A constant heat flux of 500 W m^{-2} was applied to the back face of the panel while the top face was open to convection and radiation. The emissivity was 0.97 based on the vendor value for the matte black paint on the top face, while the convection coefficient was h = 8 W m^{-2} K based on fitting to experimental data. The sidewalls of the panel were insulated and coolant circulated through the channel network at a set flow rate and inlet temperature of 22 °C (as measured at inlet thermocouples). A full list of panel dimensions, boundary conditions and material properties is given in Table 1.

To provide bounds for pressure predictions, two sets of channel dimensions were simulated: one with average channel dimensions and one with dimensions reduced by one standard deviation. For all panels but one, the average channel dimensions were 1020 μm × 840 μm and the reduced dimensions were 940 μm × 800 μm. For the bifurcating panel with smaller channels, the average dimensions were 570 μm × 500 μm and the reduced dimensions were 500 μm × 490 μm. Since the pumping pressure scales with the 4th power of the diameter, any slight restriction in channel dimension can dramatically influence the pressure prediction. We use these two simulation conditions to bound the experimental data.

Table 1
Panel dimensions, boundary conditions, and material properties used for fluent simulations.

Simulation Condition	Value
Panel dimensions in mm	
Panel width	150
Panel height	200
Panel thickness	3
Channel width	1.02[a]
Channel thickness	0.84[a]
Boundary conditions	
Total coolant flow rate (mL min^{-1})	28.2[b]
Coolant inlet temperature (°C)	22
Coolant outlet pressure (Pa)	0
Supplied heat flux (W m^{-2})	500 from back[c]
Convection coefficient h for top face (W m^{-2} K^{-1})	8
Emissivity for top face	0.97
Air temperature surrounding top face (°C)	21
Sides of panel	Insulated
Coolant – 50/50 water-ethylene glycol[d]	
Density (kg m^{-3})	1065
Viscosity (kg m^{-1} s^{-1})	$0.0069 * (T/273)^{-8.3}$
Specific heat (J kg^{-1} K^{-1})	$2574.7 + 3.0655T$
Thermal conductivity (W m^{-1} K^{-1})	0.419
Panel – Carbon fiber reinforced epoxy[e]	
Fiber volume fraction V_f (%)	45
Density (kg m^{-3})	1410
Specific heat (J kg^{-1} K^{-1})	890
In-plane thermal conductivity (W m^{-1} K^{-1})	2.04
Transverse thermal conductivity (W m^{-1} K^{-1})	0.43

[a] Channel dimensions of 0.94 mm wide × 0.80 mm thick were also simulated to provide bounds for pressure. For one panel with smaller channels, dimensions of 0.57 mm × 0.50 mm and 0.50 mm × 0.49 mm were simulated.
[b] This is the baseline value: other values also tested.
[c] This is the average value for heat flux; see Fig. 5 for distribution.
[d] Properties taken from [43].
[e] Properties determined using constituent properties and V_f. Constituent properties are given in Table S1. Density, specific heat, and in-plane conductivity were determined with rule of mixtures. Transverse conductivity was determined with the self-consistent model; see [27] for conductivity calculations.

The polyimide resistive heater used in experiments provided a slightly nonuniform heat flux (Fig. 5a). To account for this nonuniformity, a 4th-order polynomial for heat flux was fit to the IR temperature data using MATLAB (see Section S1 for details) and the polynomial was used in Fluent simulations (Fig. 5b).

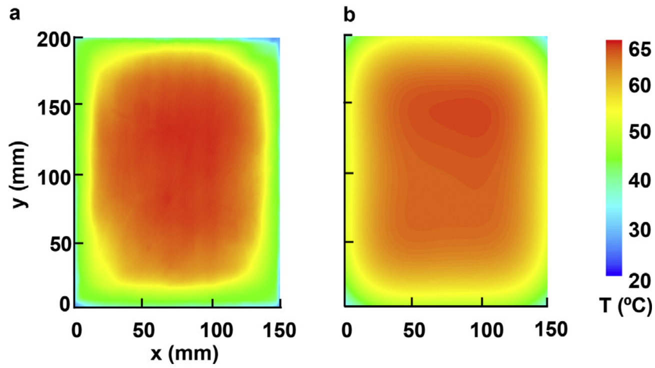

Fig. 5. Heater characterization used in cooling tests. (a) Steady-state IR surface temperature profile of the heater for a nominal heat flux of 500 W m^{-2}. (b) Simulated temperature profile of the heater with a non-uniform heat flux obtained from a 4th-order polynomial fit of the experimental temperature field.

2.2.2. Mesh generation and convergence

Tetrahedral finite volume meshes of panels were constructed in ANSYS Meshing v15.0. To test for convergence, meshes were created at successively smaller grid sizes for the parallel network design with a channel size of 1020 μm × 840 μm. The fluid element sizing had by far the greatest influence on convergence, with a 170 μm sizing required for convergence of temperature (within 0.1 °C) and pressure (within 2%, see Fig. S4). Fig. S5 displays the mesh with a 170 μm sizing that was used for future simulations. Critical fluid element sizes of 130 μm, 100 μm, and 80 μm were then found for channel sizes of 940 μm × 800 μm, 570 μm × 500 μm, and 500 μm × 490 μm respectively. The final meshes contained between 1.1–3.2 million fluid elements and 6.3–17.3 million total elements.

Steady-state simulations were performed using the SIMPLE pressure-velocity coupling scheme, Green-Gauss node-based gradient discretization, second-order pressure discretization, third-order MUSCL momentum discretization, and third-order MUSCL energy discretization. These simulations solve for the conservation of mass, momentum, and energy for an incompressible Newtonian fluid with laminar flow. The maximum Reynolds number for any simulation was ca. 500, confirming the assumption of laminar flow. The convergence criterion used was for velocity and continuity residuals to reach 10^{-3} and for the energy residual to reach 10^{-8}. These thresholds were sufficient for convergence of temperature and pressure fields.

3. Results and discussion

3.1. Thermal and pressure targets for cooling panels

The heater size and supplied heat flux were chosen to represent batteries in the Chevy Volt [42–44]. Tests were performed with the assumption of a 1:1 battery:cooling panel ratio (e.g. the stacking sequence in Fig. 1b), so the heater was powered sufficiently to provide a heat flux representative of one battery in the Volt (500 W m^{-2} nominal). The choice of coolant (50:50 water:ethylene glycol) and baseline flow rate (28.2 mL min^{-1}, or 0.5 g s^{-1}) were also chosen to match the Volt cooling system [42–44].

The goal for a battery cooling panel is to minimize panel temperature since lower battery temperature leads to reduced side reactions and longer lifetime [3,4]. The standard deviation of temperature across the panel, σ_T, should also be minimized since variations in battery temperature lead to uneven charge/discharge profiles across the battery. Finally, pressure should be minimized to reduce pumping power. Current vehicle cooling systems typically operate at pressures of <120 kPa [50].

3.2. Effect of flow rate

The effect of flow rate on cooling performance was first investigated for the parallel network panel (Fig. 6). With no coolant flow, maximum surface temperature T_{max} reaches approximately 60 °C. As flow rate increases, T_{max} drops quickly as heat is removed by the coolant and then reaches a plateau value. Average surface temperature T_{av} and σ_T similarly decrease and plateau for increasing flow rate (see Table 2). Higher flow rates result in smaller values of ΔT_c as the outlet coolant temperature approaches the inlet temperature (Table 2). Cooling efficiency η improves with flow rate and then plateaus reaching roughly 75% at the highest flow rate tested (56.4 mL min^{-1}) (Fig. 6). Good agreement was obtained between experimental data and simulations for surface temperature profiles and cooling efficiency. Small discrepancies between experimental and simulated values are likely due to experimental error or variation of the convection coefficient (see discussion in Section S2).

Pumping pressure rises almost linearly with flow rate (Fig. 7a). Any nonlinearity is attributed to pressure losses at corners and at locations where fluid streams combine and separate [51]. The maximum pressure measured (25 kPa) is well within the range of commercial coolant pumps. Two sets of simulations were performed in order to bound the pumping pressure. The first used nominal (average) dimensions for the channel cross-section (1020 μm × 840 μm). A second simulation was performed using a cross-section of 940 μm × 800 μm which represents one standard deviation below nominal. Given the extreme sensitivity of pressure with respect to hydraulic diameter, any decrease in nominal cross-sectional area can lead to a large increase in pressure. Both simulations bound the experimental data well.

Pumping power was calculated by multiplying coolant pressure by volumetric flow rate and is plotted in Fig. 7b. The power increases with the square of the flow rate as expected. The magnitude of pumping power is small at all flow rates considered and well within available power limits for an EV battery.

3.3. Effect of network design

3.3.1. Thermal performance

Four different vascular networks with similar volume and inter-channel spacing (Fig. 3) were fabricated for comparison studies. Two branched networks (parallel and bifurcating) and two single-channel networks (serpentine and spiral) were chosen, inspired by prior cooling studies for batteries and fuel cells [43–48]. Cooling panels with each of these networks were tested at 28.2 mL min^{-1} flow rate for comparison (Fig. 8). Simulated and experimental temperature profiles agree well in all cases. For all networks, hot spots form between cooling channels due to relatively slow heat conduction to the channel surface. Temperature generally increases in the direction of coolant flow due to heat transfer into the coolant. Both T_{av} and ΔT_c are similar for all panel designs (Table 2).

Both T_{max} and σ_T are more affected by network design (Fig. 9). The parallel network has the highest values of T_{max} and σ_T since it develops a large hot spot near the center of the panel. Simulations suggest the hot spot forms due to uneven flow distribution, with the least flow moving through the center of the panel (Fig. 10). In contrast, the bifurcating network shows a very uniform flow distribution and correspondingly better thermal performance.

The serpentine network shows slightly better thermal performance than the bifurcating network, likely due to the presence of counter flow in adjacent branches of the network. The spiral network has the best thermal performance of all designs considered, with the lowest T_{max} and σ_T. This is likely because the coolant

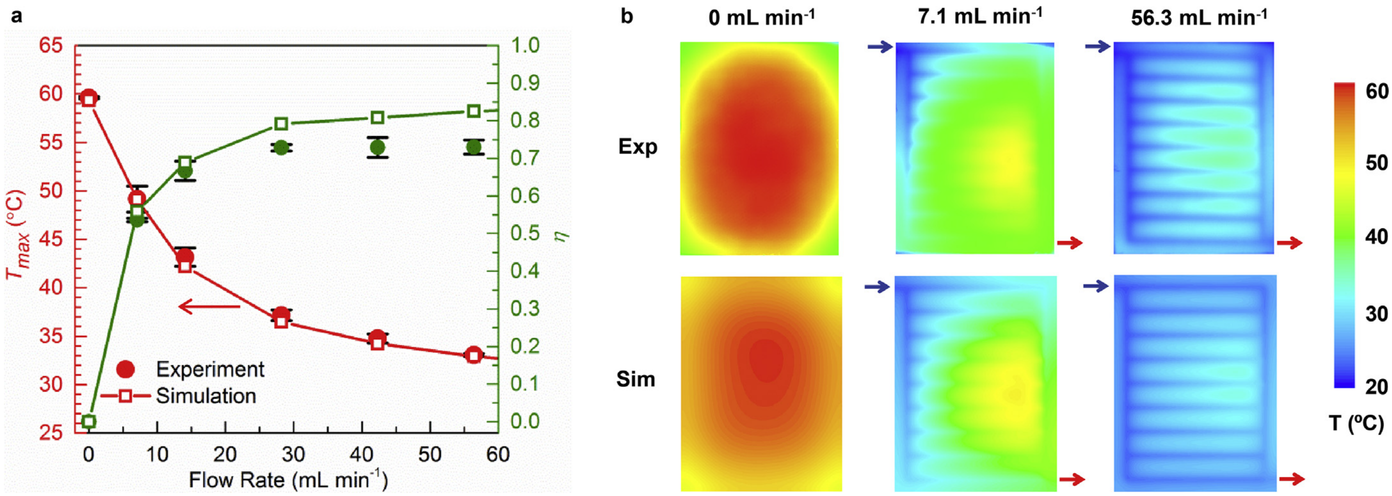

Fig. 6. Effect of flow rate on cooling performance for the parallel network panel. (a) Maximum panel temperature T_{max} and cooling efficiency η as a function of flow rate. Error bars represent the maximum and minimum values for two replicate panels. (b) Experimental and simulated surface temperature profiles at various flow rates. Inlet and outlet locations are denoted by blue (→) and red arrows (→). Simulations were performed using nominal channel dimensions. (For interpretation of the references to colour in this figure legend, the reader is referred to the web version of this article.)

Table 2
Values of average surface temperature T_{av}, maximum surface temperature T_{max}, standard deviation of surface temperature σ_T, and coolant temperature rise ΔT_c for all experiments. Simulated values using nominal dimensions are shown for comparison. Experimental variation gives the maximum and minimum values for replicate panels.

Network	Channel volume fraction (%)	Samples tested	Flow rate (ml min^{-1})	T_{av} (°C)		T_{max} (°C)		σ_T (°C)		ΔT_c (°C)	
				Sim.	Exp.	Sim.	Exp.	Sim.	Exp.	Sim.	Exp.
Parallel	1.5	2	0	55.1	53.6 ± 0.1	59.3	59.6 ± 0.2	2.9	4.4 ± 0.3	N/A	N/A
	1.5	2	7.1	36.7	37.9 ± 1.0	49.1	49.2 ± 1.4	6.6	6.2 ± 0.4	19.0	18.3 ± 0.2
	1.5	2	14.1	32.1	33.7 ± 0.6	42.2	43.2 ± 1.0	4.7	4.5 ± 0.3	11.8	11.4 ± 0.4
	1.5	2	28.2	29.0	30.4 ± 0.2	36.5	37.2 ± 0.6	3.2	3.0 ± 0.3	6.8	6.2 ± 0.1
	1.5	2	42.3	28.0	29.2 ± 0.2	34.2	34.8 ± 0.5	2.6	2.4 ± 0.2	4.6	4.2 ± 0.2
	1.5	2	56.4	27.4	28.4 ± 0.1	32.9	33.1 ± 0.2	2.3	2.0 ± 0.1	3.5	3.1 ± 0.1
Bifurcating	1.5	2	28.2	28.8	30.5 ± 0.2	33.0	35.1 ± 0.5	2.5	2.6 ± 0.2	6.7	7.0 ± 0.1
Serpentine	1.3	2	28.2	28.6	29.9 ± 0.1	32.6	33.8 ± 0.2	2.1	2.3 ± 0.3	6.8	6.4 ± 0.2
Spiral	1.4	2	28.2	28.4	30.0 ± 0.2	31.5	33.2 ± 0.1	1.9	1.8 ± 0.1	6.8	6.7 ± 0.2
Bifurcating[a]	0.5	1	28.2	29.2	30.8	33.3	35.6	2.5	2.8	6.8	7.2
Optimized	1.6	1	28.2	28.4	29.7	33.1	33.9	2.3	2.4	6.8	6.9

[a] Bifurcating network with channel size of 570 μm × 500 μm, vs. 1020 μm × 840 μm channel size for all other samples.

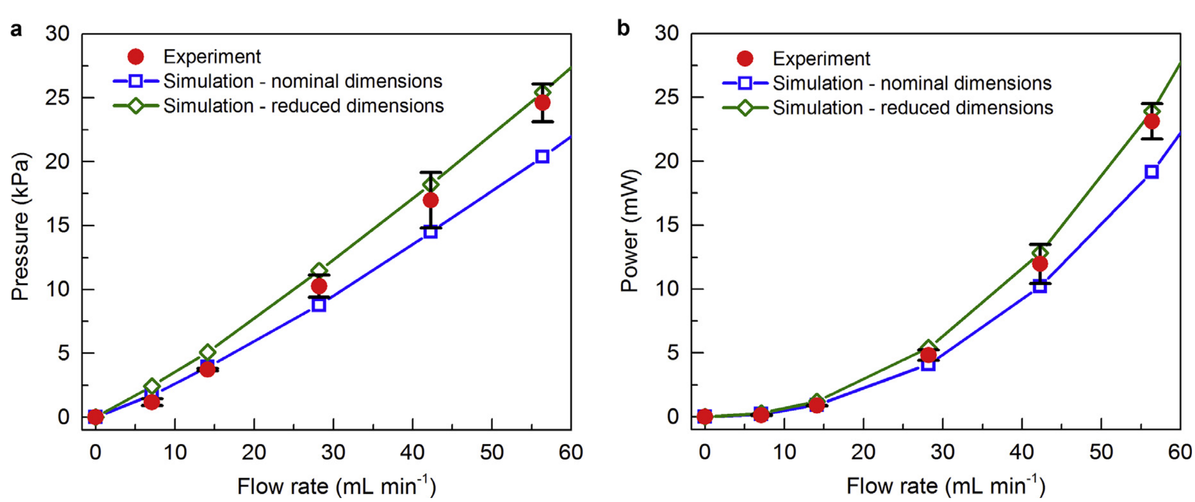

Fig. 7. Pumping pressure and power for the parallel network panel. (a) Experimental and simulated pressure vs. flow rate and (b) power vs. flow rate. Simulations are performed using the average channel dimensions (1020 μm × 840 μm) and dimensions reduced by one standard deviation (940 μm × 800 μm). Error bars represent the maximum and minimum values for two replicate panels.

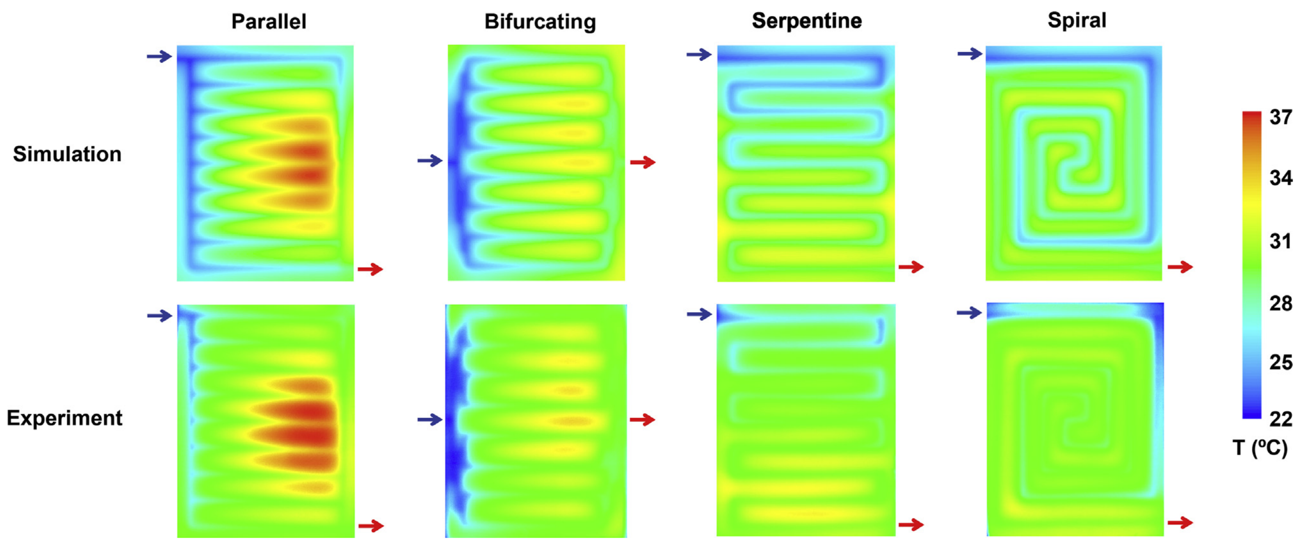

Fig. 8. Experimental and simulated surface temperature profiles for the four vascular network designs at a flow rate of 28.2 mL min^{-1}. Inlet and outlet locations are denoted by blue (→) and red arrows (→). Simulations were performed with nominal channel dimensions. (For interpretation of the references to colour in this figure legend, the reader is referred to the web version of this article.)

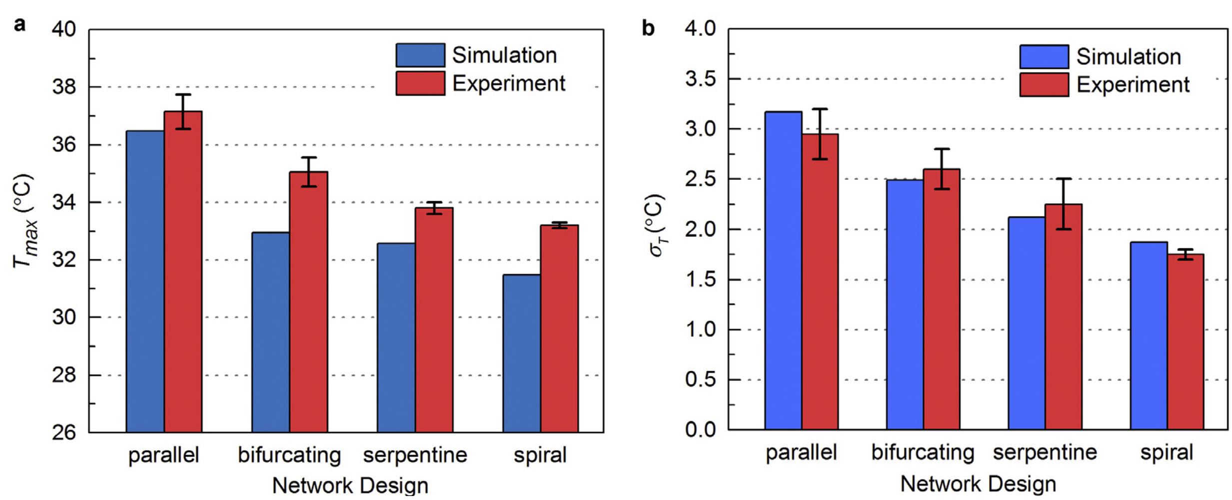

Fig. 9. Comparison of thermal performance for all network designs. (a) Maximum surface temperature T_{max} and (b) standard deviation of surface temperature σ_T, with error bars representing maximum and minimum values for 2 replicate panels. The flow rate is 28.2 mL min^{-1} for all cases. Simulations were performed with nominal channel dimensions.

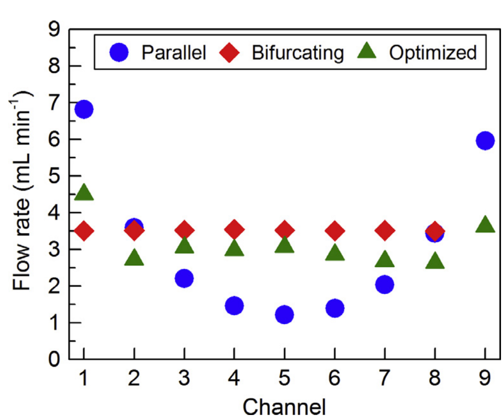

Fig. 10. Simulated flow rate distribution through branched networks at 28.2 mL min^{-1} total flow rate. The channels are numbered from top to bottom of the panel. Simulations were performed with nominal channel dimensions.

moves around the periphery, mitigating the thermal hot spot at the outlet location of the serpentine design.

3.3.2. Pressure performance

The parallel and bifurcating networks have similar pumping pressures at 28.2 mL min^{-1} flow rate and are quite low in magnitude (8–10 kPa) (Fig. 11). The serpentine and spiral networks require pumping pressures that are an order of magnitude higher (100–110 kPa) and approaching the upper limit of typical vehicle coolant pumps. This large disparity in required pressure is a result of the division of flow in the branched networks, which results in both shorter channel lengths and lower flow rate within each channel. Nevertheless, pumping power requirements for the serpentine and spiral networks are low in magnitude (<60 mW).

Considering both temperature and pressure objectives, the spiral and bifurcating network designs offer the best overall performance. The spiral network offers the best thermal performance at feasible pumping pressures. However, the bifurcating network is likely a better overall choice since it has nearly comparable ther-

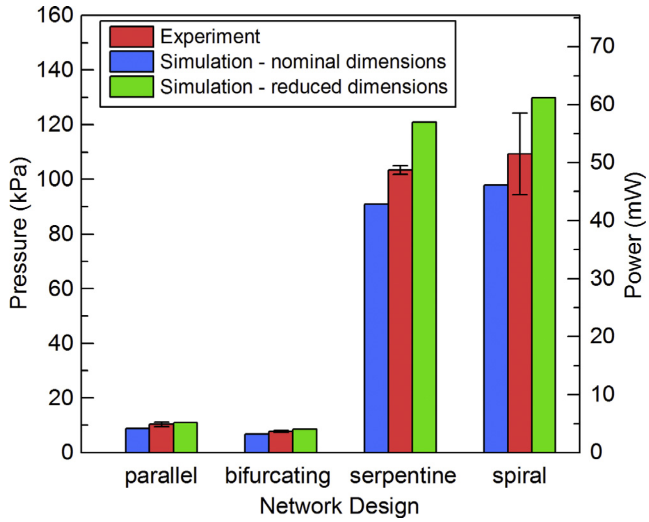

Fig. 11. Pumping pressure and power for the four network designs evaluated at 28.2 mL min^{-1}. Simulations were performed using average channel dimensions (1020 μm × 840 μm) and channel dimensions reduced by one standard deviation (940 μm × 800 μm). Error bars represent the maximum and minimum values for two replicate panels.

mal performance, but at much lower pumping pressures. The lower required pumping pressure means that higher flow rates could be easily accessed to improve thermal performance. The presence of multiple channels offers redundancy to mitigate the effect of channel blockages. In addition, the bifurcating network can easily be modified to accommodate more channels (e.g. 16 channels instead of 8), which would increase channel density and decrease the panel temperature as was previously shown for 1D channels [42]. Conversely, it would be difficult to increase channel density for both the serpentine and spiral networks since this would increase the overall channel length and required pumping pressure.

3.4. Effect of channel size

The nominal channel size investigated (1020 μm × 840 μm) is similar to those used in commercial (aluminum) cooling panels. Smaller channels can be advantageous for composite panels, however, since they are less likely to disrupt fiber architecture and thus, less likely to reduce mechanical properties [36]. To demonstrate the use of smaller channels, a bifurcating network panel was fabricated with a channel size of 570 ± 70 μm wide and 500 ± 10 μm tall. The panel was tested at a flow rate of 28.2 mL min^{-1} and gives a nearly identical thermal profile to the bifurcating network panel with larger channels (see Fig. S6 and Table 2). The penalty for using smaller channels is that pumping pressure increases significantly from ~8 kPa for the larger channel network to ~60 kPa for the smaller channel network. However, the required pressure is still well within the range of commercial pumps.

3.5. Improvements in channel design using gradient-based optimization

The four network designs presented in Fig. 3 were selected *a priori*, but improved performance can be obtained through computational optimization. The standard finite element method (FEM) is poorly suited for optimizing microchannel networks, since conforming meshes are needed to capture discontinuous temperature gradients across fluid/solid interfaces. The need for a conforming mesh leads to long meshing/simulation times and can cause mesh distortion as the microchannel configuration evolves. More efficient optimization can be achieved using the interface-enriched generalized finite element method (IGFEM), in which interface enrichment functions are used to capture discontinuous temperature gradients with a nonconforming mesh [52]. The IGFEM thus allows for an efficient optimization of microvascular materials using a single, nonconforming mesh [33]. The IGFEM can be further improved by using the hierarchical interface-enriched finite element method (HIFEM), which allows for the simulation of multiple phase boundaries in a single mesh element [53], and by using non-uniform rational B-splines (NURBS) to define complex microchannel geometries [54,55].

In Tan et al. [49], IGFEM was combined with a shape sensitivity solver and a gradient-based optimization scheme to improve the thermal performance of panels. The network nodes defining the embedded microchannel network were iteratively moved within the panel in order to reduce the maximum temperature of the panel. Computational efficiency was further enhanced by using dimensionally-reduced thermal and hydraulics models to calculate temperature and pressure fields.

A panel with the optimized parallel network (Fig. 12a) was fabricated and compared in performance to the nominal parallel network design. The optimal network design features diagonal channels that branch off closer to the channel inlet than the nominal parallel design. This yields a more uniform flow distribution through the branches (Fig. 10) and a correspondingly lower panel temperature (Fig. 12b and c). The required pumping pressure through the optimal network was nearly unchanged from the nominal design (Fig. S7).

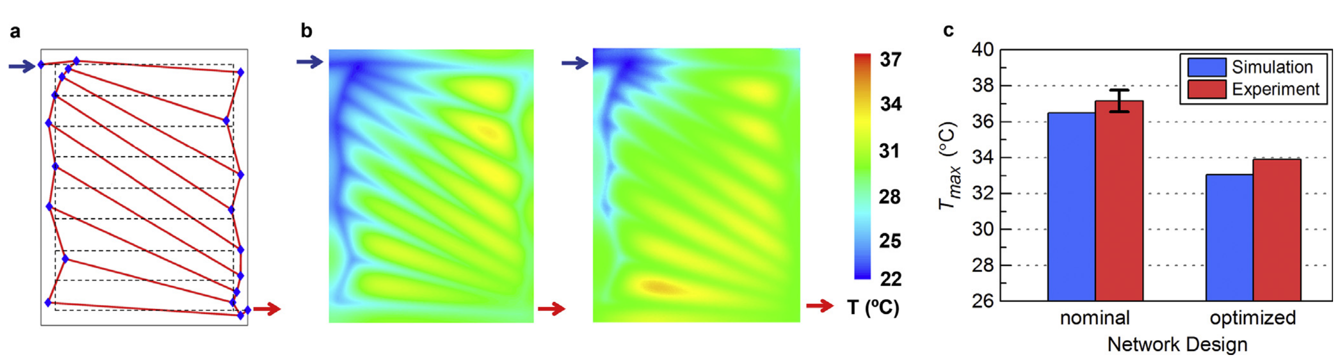

Fig. 12. Thermal performance for an optimized version of the parallel network design. (a) Optimal network design (minimum temperature) from gradient-based optimization scheme [49] of the placement of network nodes. The original (parallel) network is shown in black while the optimized network is shown in red. (b) Simulated (left) and experimental (right) surface temperature profiles of the optimized network at a flow rate of 28.2 mL min^{-1}. Inlet and outlet locations are denoted by blue (→) and red arrows (→). (c) Comparison of T_{max} for the nominal and optimized designs. Error bars for the nominal panel represent the maximum and minimum values for two replicate panels. Simulations were performed with nominal channel dimensions.

Table 3
Modifications to the values in Table 1 for simulation of a cooling panel in an EV battery pack.

Simulation condition	Modified value
Boundary conditions	
Coolant inlet temperature (°C)	27
Supplied heat flux (W m^{-2})	250 from top and 250 from bottom [a]
Panel – Carbon fiber reinforced epoxy	
Fiber volume fraction (%)	60
Density (kg m^{-3})	1500
Specific heat (J kg^{-1} K^{-1})	860
In-plane thermal conductivity (W m^{-1} K^{-1})	2.7
Transverse thermal conductivity (W m^{-1} K^{-1})	0.59

[a] For the baseline case of 500 W m^{-2} total, the nonuniform heat flux from Fig. 5 was simulated but with half the magnitude applied to both sides. Other total heat flux values were also simulated by linearly scaling the heat flux distribution.

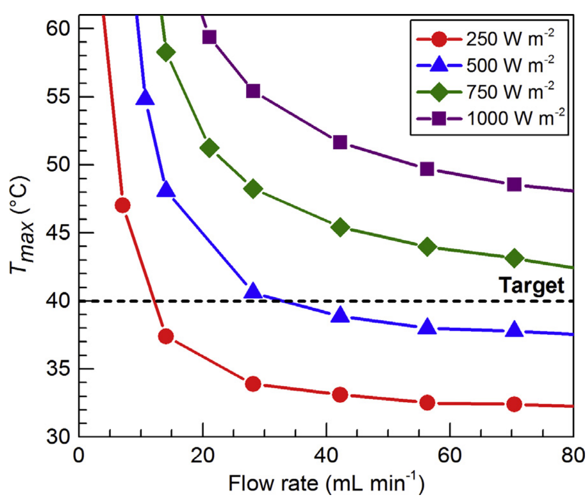

Fig. 13. Thermal performance of a panel with the optimized network design subject to EV battery pack conditions (see Table 3) and different flow rate. The legend denotes the total applied heat flux which is evenly divided between both sides (top and bottom) of the cooling panel.

3.6. Simulations more closely representing an EV battery pack

The Fluent simulations in Sections 3.2–3.5 were validated by experimental correlation. However, cooling panels in an actual battery pack would be heated by batteries from both sides (see Fig. 1b) instead of having one face open to convection/radiation. In addition, the coolant inlet temperature would likely be higher than room temperature [43,44] and commercial composite panels would be manufactured at higher fiber volume fraction, giving higher thermal conductivity. Simulations were performed with these changes (Table 3) for the optimized network design. Again, the cooling objective was to maintain T_{max} below 40 °C.

For a total applied heat flux of 500 W m^{-2}, the panel reaches $T_{max} \approx 40$ °C at a flow rate of approximately 30 mL min^{-1} (Fig. 13). Thus, the panel reaches the target temperature near the baseline flow rate as desired. For a supplied heat flux of 250 W m^{-2}, which is representative of lower power batteries or a stacking sequence where there are two panels per battery, a flow rate of only ~15 mL min^{-1} is required. For higher heat fluxes of 750 and 1000 W m^{-2}, the panel cannot reach the target temperature for the flow rates investigated. However, the target temperature would likely be reached by increasing the density of the channel network as was previously shown for panels with 1D channels [42].

4. Conclusions

Microvascular carbon fiber/epoxy composites could represent a new class of strong, lightweight, thermally responsive battery packaging materials. The VaSC processing technique enables the fabrication of composites with complex, 2D, interconnected vascular networks. Composite panels with a variety of different vascular networks were fabricated and tested under an applied heat flux (500 W m^{-2}) and coolant flow rate (28.2 mL min^{-1}) representative of typical EV battery cooling conditions. The spiral network offers the best thermal performance with relatively high pumping pressure (>100 kPa) while the bifurcating network offers good thermal performance at much reduced pressure (<10 kPa). Large hot spots form on panels with the nominal parallel network, but these hot spots can be reduced by modifying the network with a gradient-based optimization scheme. Panel cooling performance was unaffected by channel size.

CFD simulations were validated by experiment for all panels and operating conditions tested. Further simulations confirm that composite panels can sufficiently cool an EV battery pack below 40 °C. Work is ongoing to design carbon fiber cooling panels for fuel cells, microelectronics, antennas [56], and satellites [57]. Future studies should also investigate the impact that 2D channel networks have on composite mechanical properties.

Conflict of interest

The authors declared that there is no conflict of interest.

Acknowledgements

This research was supported by the National Science Foundation (CMMI 14-36720). SJP was supported by DOD, AFOSR, National Defense Science and Engineering Graduate (NDSEG) Fellowship, 32 CFR 168a. The authors extend gratitude to Tony Coppola, Kevin Hart, Ryan Gergely, Sang Yup Kim, and Quinn Calvert for composite manufacture and testing, Prof. Nancy Sottos for helpful discussion, and Travis Ross of the Beckman Visualization Laboratory for help with ANSYS Fluent.

Appendix A. Supplementary material

Supplementary data associated with this article can be found, in the online version, at http://dx.doi.org/10.1016/j.ijheatmasstransfer.2017.07.047.

References

[1] E. Schuster, C. Ziebert, A. Melcher, M. Rohde, H.J. Seifert, Thermal behavior and electrochemical heat generation in a commercial 40 Ah lithium ion pouch cell, J. Power Sourc. 286 (2015) 580–589.
[2] G.-H. Kim, K. Smith, K.-J. Lee, S. Santhanagopalan, A. Pesaran, Multi-domain modeling of lithium-ion batteries encompassing multi-physics in varied length scales, J. Electrochem. Soc. 158 (2011) A955.
[3] T.M. Bandhauer, S. Garimella, T.F. Fuller, A critical review of thermal issues in lithium-ion batteries, J. Electrochem. Soc. 158 (2011) R1.
[4] J. Neubauer, E. Wood, Thru-life impacts of driver aggression, climate, cabin thermal management, and battery thermal management on battery electric vehicle utility, J. Power Sourc. 259 (2014) 262–275.
[5] D.P. Finegan, M. Scheel, J.B. Robinson, B. Tjaden, I. Hunt, T.J. Mason, J. Millichamp, M. Di Michiel, G.J. Offer, G. Hinds, D.J.L. Brett, P.R. Shearing, In-operando high-speed tomography of lithium-ion batteries during thermal runaway, Nat. Commun. 6 (2015) 6924.
[6] S. Jayaraman, G. Anderson, S. Kaushik, P. Klaus, Modeling of Battery Pack Thermal System for a Plug-in Hybrid Electric Vehicle, SAE Tech. Rep. 2011-01-0666, 2011.
[7] H.S. Hamut, I. Dincer, G.F. Naterer, Experimental and theoretical efficiency investigation of hybrid electric vehicle battery thermal management systems, J. Energy Resour. Technol. 136 (2014) 11202.

[8] F. He, X. Li, L. Ma, Combined experimental and numerical study of thermal management of battery module consisting of multiple Li-ion cells, Int. J. Heat Mass Transf. 72 (2014) 622–629.
[9] B. Severino, F. Gana, R. Palma-Behnke, P.A. Estévez, W.R. Calderón-Muñoz, M.E. Orchard, J. Reyes, M. Cortés, Multi-objective optimal design of lithium-ion battery packs based on evolutionary algorithms, J. Power Sourc. 267 (2014) 288–299.
[10] A. Greco, D. Cao, X. Jiang, H. Yang, A theoretical and computational study of lithium-ion battery thermal management for electric vehicles using heat pipes, J. Power Sourc. 257 (2014) 344–355.
[11] R. Kizilel, R. Sabbah, J.R. Selman, S. Al-Hallaj, An alternative cooling system to enhance the safety of Li-ion battery packs, J. Power Sourc. 194 (2009) 1105–1112.
[12] B. Smith, Chevrolet Volt Battery Incident Overview Report, Technical Report DOT HS 811573, 2012. http://www-odi.nhtsa.dot.gov/acms/cs/jaxrs/download/doc/UCM399393/INRP-PE11037-49880.pdf (accessed January 6, 2017).
[13] A. Aylor, Chevrolet Volt Battery Pack Tests, Technical Report GTL-DOT-11-VOLTBAT 2012, 2012. http://www.jensenhughes.com/wp-content/uploads/2014/02/White_Paper_Chevy-Volt-Batterye-Pack-Tests_USDOT-NHTSA_AAylor-GBack-CWinchester_JAN-2012.pdf (accessed January 6, 2017).
[14] L.E. Asp, E.S. Greenhalgh, Structural power composites, Compos. Sci. Technol. 101 (2014) 41–61.
[15] J. Thomas, S. Qidwai, W. Pogue, G. Pham, Multifunctional structure-battery composites for marine systems, J. Compos. Mater. 47 (2012) 5–26.
[16] D.H.-J.A. Lukaszewicz, Automotive composite structures for crashworthiness, in: A. Elmarakbi (Ed.), Adv. Compos. Mater. Automot. Appl. Struct. Integr. Crashworthiness, John Wiley & Sons, Ltd, Chichester, 2014, pp. 99–127.
[17] A. Kousourakis, A.P. Mouritz, The effect of self-healing hollow fibres on the mechanical properties of polymer composites, Smart Mater. Struct. 19 (2010) 85021.
[18] M.-U. Saeed, Z. Chen, B. Li, Manufacturing strategies for microvascular polymeric composites: a review, Compos. Part A Appl. Sci. Manuf. 78 (2015) 327–340.
[19] D.T. Everitt, T.S. Coope, R.S. Trask, D.F. Wass, I.P. Bond, Application of a silver–olefin coordination polymer as a catalytic curing agent for self-healing epoxy polymers, Smart Mater. Struct. 24 (2015) 55004.
[20] T.S. Coope, D.F. Wass, R.S. Trask, I.P. Bond, Repeated self-healing of microvascular carbon fibre reinforced polymer composites, Smart Mater. Struct. 23 (2014) 115002.
[21] C.J. Norris, I.P. Bond, R.S. Trask, Interactions between propagating cracks and bioinspired self-healing vascules embedded in glass fibre reinforced composites, Compos. Sci. Technol. 71 (2011) 847–853.
[22] C.J. Norris, G.J. Meadway, M.J. O'Sullivan, I.P. Bond, R.S. Trask, Self-healing fibre reinforced composites via a bioinspired vasculature, Adv. Funct. Mater. 21 (2011) 3624–3633.
[23] A.P. Esser-Kahn, P.R. Thakre, H. Dong, J.F. Patrick, V.K. Vlasko-Vlasov, N.R. Sottos, J.S. Moore, S.R. White, Three-dimensional microvascular fiber-reinforced composites, Adv. Mater. 23 (2011) 3654–3658.
[24] J.F. Patrick, K.R. Hart, B.P. Krull, C.E. Diesendruck, J.S. Moore, S.R. White, N.R. Sottos, Continuous self-healing life cycle in vascularized structural composites, Adv. Mater. 26 (2014) 4302–4308.
[25] R.C.R. Gergely, S.J. Pety, B.P. Krull, J.F. Patrick, T.Q. Doan, A.M. Coppola, P.R. Thakre, N.R. Sottos, J.S. Moore, S.R. White, Multidimensional vascularized polymers using degradable sacrificial templates, Adv. Funct. Mater. 25 (2015) 1043–1052.
[26] A.M. Coppola, P.R. Thakre, N.R. Sottos, S.R. White, Tensile properties and damage evolution in vascular 3D woven glass/epoxy composites, Compos. Part A Appl. Sci. Manuf. 59 (2014) 9–17.
[27] A.M. Coppola, A.S. Griffin, N.R. Sottos, S.R. White, Retention of mechanical performance of polymer matrix composites above the glass transition temperature by vascular cooling, Compos. Part A Appl. Sci. Manuf. 78 (2015) 412–423.
[28] A.M. Coppola, L. Hu, P.R. Thakre, M. Radovic, I. Karaman, N.R. Sottos, S.R. White, Active cooling of a microvascular shape memory alloy-polymer matrix composite hybrid material, Adv. Eng. Mater. 18 (2016) 1145–1153.
[29] A.M. Coppola, L.G. Warpinski, S.P. Murray, N.R. Sottos, S.R. White, Survival of actively cooled microvascular polymer matrix composites under sustained thermomechanical loading, Compos. Part A Appl. Sci. Manuf. 82 (2016) 170–179.
[30] D.M. Phillips, M. Ryan Pierce, J.W. Baur, Mechanical and thermal analysis of microvascular networks in structural composite panels, Compos. Part A Appl. Sci. Manuf. 42 (2011) 1609–1619.
[31] M.W. McElroy, A. Lawrie, I.P. Bond, Optimisation of an air film cooled CFRP panel with an embedded vascular network, Int. J. Heat Mass Transf. 88 (2015) 284–296.
[32] S. Soghrati, A.R. Najafi, J.H. Lin, K.M. Hughes, S.R. White, N.R. Sottos, P.H. Geubelle, Computational analysis of actively-cooled 3D woven microvascular composites using a stabilized interface-enriched generalized finite element method, Int. J. Heat Mass Transf. 65 (2013) 153–164.
[33] A.R. Najafi, M. Safdari, D.A. Tortorelli, P.H. Geubelle, A gradient-based shape optimization scheme using an interface-enriched generalized FEM, Comput. Methods Appl. Mech. Eng. 296 (2015) 1–17.
[34] C.J. Hansen, Microvascular-based self-healing materials, in: G. Li, H. Meng (Eds.), Recent Adv. Smart Self-Healing Polym. Compos., Elsevier Ltd., Cambridge, 2015, pp. 129–157.
[35] N. Sakurayama, S. Minakuchi, N. Takeda, Sensing and healing of disbond in composite stiffened panel using hierarchical system, Compos. Struct. 132 (2015) 833–841.
[36] M. Saeed, B. Li, Z. Chen, Mechanical effects of microchannels on fiber-reinforced composite structure, Compos. Struct. 154 (2016) 129–141.
[37] A. Kousourakis, M.K. Bannister, A.P. Mouritz, Tensile and compressive properties of polymer laminates containing internal sensor cavities, Compos. Part A Appl. Sci. Manuf. 39 (2008) 1394–1403.
[38] C.-Y. Huang, R.S. Trask, I.P. Bond, Characterization and analysis of carbon fibre-reinforced polymer composite laminates with embedded circular vasculature, J. R. Soc. Interf. 7 (2010) 1229–1241.
[39] D.J. Hartl, G.J. Frank, J.W. Baur, Effects of microchannels on the mechanical performance of multifunctional composite laminates with unidirectional laminae, Compos. Struct. 143 (2016) 242–254.
[40] C.J. Norris, I.P. Bond, R.S. Trask, The role of embedded bioinspired vasculature on damage formation in self-healing carbon fibre reinforced composites, Compos. Part A Appl. Sci. Manuf. 42 (2011) 639–648.
[41] A. Kousourakis, A.P. Mouritz, M.K. Bannister, Interlaminar properties of polymer laminates containing internal sensor cavities, Compos. Struct. 75 (2006) 610–618.
[42] S.J. Pety, Microvascular Composites as a Multifunctional Material for Electric Vehicles, PhD Thesis, University of Illinois at Urbana-Champaign, 2017.
[43] A. Jarrett, I.Y. Kim, Design optimization of electric vehicle battery cooling plates for thermal performance, J. Power Sourc. 196 (2011) 10359–10368.
[44] A. Jarrett, I.Y. Kim, Influence of operating conditions on the optimum design of electric vehicle battery cooling plates, J. Power Sourc. 245 (2014) 644–655.
[45] J.C. Kurnia, A.P. Sasmito, A.S. Mujumdar, Numerical investigation of laminar heat transfer performance of various cooling channel designs, Appl. Therm. Eng. 31 (2011) 1293–1304.
[46] G. Zhang, S.G. Kandlikar, A critical review of cooling techniques in proton exchange membrane fuel cell stacks, Int. J. Hydrogen Energy 37 (2012) 2412–2429.
[47] S. Ravishankar, K. Arul Prakash, Numerical studies on thermal performance of novel cooling plate designs in polymer electrolyte membrane fuel cell stacks, Appl. Therm. Eng. 66 (2014) 239–251.
[48] B. Ramos-Alvarado, P. Li, H. Liu, A. Hernandez-Guerrero, CFD study of liquid-cooled heat sinks with microchannel flow field configurations for electronics, fuel cells, and concentrated solar cells, Appl. Therm. Eng. 31 (2011) 2494–2507.
[49] M.H.Y. Tan, A.R. Najafi, S.J. Pety, S.R. White, P.H. Geubelle, Gradient-based design of actively-cooled microvascular composite panels, Int. J. Heat Mass Transf. 103 (2016) 594–606.
[50] T. Gilles, Automotive Service: Inspection, Maintenance, Repair, fourth ed., Cengage Learning, New York, 2012.
[51] D. Haller, P. Woias, N. Kockmann, Simulation and experimental investigation of pressure loss and heat transfer in microchannel networks containing bends and T-junctions, Int. J. Heat Mass Transf. 52 (2009) 2678–2689.
[52] S. Soghrati, P.H. Geubelle, A 3D interface-enriched generalized finite element method for weakly discontinuous problems with complex internal geometries, Comput. Methods Appl. Mech. Eng. 217–220 (2012) 46–57.
[53] S. Soghrati, H. Ahmadian, 3D hierarchical interface-enriched finite element method: implementation and applications, J. Comput. Phys. 299 (2015) 45–55.
[54] M.H.Y. Tan, M. Safdari, A.R. Najafi, P.H. Geubelle, A NURBS-based interface-enriched generalized finite element scheme for the thermal analysis and design of microvascular composites, Comput. Methods Appl. Mech. Eng. 283 (2015) 1382–1400.
[55] S. Soghrati, R. Alvarez, NURBS enhanced HIFEM: a fully mesh-independent method with zero geometric discretization error, Finite Elem. Anal. Des. 120 (2016) 68–79.
[56] D.J. Hartl, G.J. Frank, G.H. Huff, J.W. Baur, A liquid metal-based structurally embedded vascular antenna: I. Concept and multiphysical modeling, Smart Mater. Struct. 26 (2017) 25002.
[57] D.T. Bunce, K.P. Bassett, A.R.M. Ghosh, P.R. Barnett, D.M. Haken, S. Vrkljan, R. Jagannatha, T. Silva, V.L. Coverstone, Microvascular composite radiators for small spacecraft thermal management systems, in: Proc. 30th Annu. AIAA/USU Conf. Small Satell., 2016, p. SSC16-X-1.